The Astrophysical Journal, 926:68 (14pp), 2022 February 10 https://doi.org/10.3847/1538-4357/ac41c2

Gaia 20eae: A Newly Discovered Episodically Accreting Young Star

Arpan Ghosh[1,2], Saurabh Sharma[1], Joe P. Ninan[3,4], Devendra K. Ojha[5], Bhuwan C. Bhatt[6], Shubham Kanodia[3,4], Suvrath Mahadevan[3,4], Gudmundur Stefansson[7], R. K. Yadav[8], A. S. Gour[2], Rakesh Pandey[1,2], Tirthendu Sinha[1,9], Neelam Panwar[1], John P. Wisniewski[10], Caleb I. Cañas[3,4,15], Andrea S. J. Lin[3,4], Arpita Roy[11,12], Fred Hearty[3,4], Lawrence Ramsey[3,4], Paul Robertson[13], and Christian Schwab[14]

[1] Aryabhatta Research Institute of Observational Sciences (ARIES), Manora Peak, Nainital 263 001, India
[2] School of Studies in Physics and Astrophysics, Pandit Ravishankar Shukla University, Raipur 492010, Chhattisgarh, India
[3] Department of Astronomy and Astrophysics, The Pennsylvania State University, 525 Davey Laboratory, University Park, PA 16802, USA
[4] Center for Exoplanets and Habitable Worlds, The Pennsylvania State University, 525 Davey Laboratory, University Park, PA 16802, USA
[5] Department of Astronomy and Astrophysics, Tata Institute of Fundamental Research (TIFR), Mumbai 400005, Maharashtra, India
[6] Indian Institute of Astrophys., II Block, Koramangala, Bangalore 560 034, India
[7] Princeton University, Princeton, NJ 08544, USA
[8] National Astronomical Research Institute of Thailand, Chiang Mai, 50200, Thailand
[9] Kumaun University, Nainital 263001, India
[10] Homer L. Dodge Department of Physics and Astronomy, University of Oklahoma, Norman, OK 73019, USA
[11] Space Telescope Science Institute, 3700 San Martin Drive, Baltimore, MD 21218, USA
[12] Department of Physics and Astronomy, Johns Hopkins University, 3400 North Charles Street, Baltimore, MD 21218, USA
[13] Department of Physics and Astronomy, University of California Irvine, Irvine, CA 92697, USA
[14] Department of Physics and Astronomy, Macquarie University, Balaclava Road, North Ryde, NSW 2109, Australia
Received 2021 June 25; revised 2021 November 30; accepted 2021 December 1; published 2022 February 11

Abstract

The Gaia Alert System issued an alert on 2020 August 28, on Gaia 20eae when its light curve showed a ∼4.25 magnitude outburst. We present multiwavelength photometric and spectroscopic follow-up observations of this source since 2020 August and identify it as the newest member of the FUor/EXor family of sources. We find that the present brightening of Gaia 20eae is not due to the dust-clearing event but due to an intrinsic change in the spectral energy distribution. The light curve of Gaia 20eae shows a transition stage during which most of its brightness (∼3.4 mag) has occurred on a short timescale of 34 days with a rise rate of 3 mag/month. Gaia 20eae has now started to decay at a rate of 0.3 mag/month. We have detected a strong P Cygni profile in Hα, which indicates the presence of winds originating from regions close to the accretion. We find signatures of very strong and turbulent outflow and accretion in Gaia 20eae during this outburst phase. We have also detected a redshifted absorption component in all of the Ca II IR triplet lines consistent with a signature of hot infalling gas in the magnetospheric accretion funnel. This enables us to constrain the viewing angle with respect to the accretion funnel. Our investigation of Gaia 20eae points toward magnetospheric accretion being the phenomenon for the current outburst.

Unified Astronomy Thesaurus concepts: Protoplanetary disks (1300); Variable stars (1761); Early-type stars (430); Star formation (1569); Stellar winds (1636); T Tauri stars (1681); Young stellar objects (1834)

1. Introduction

Episodic accretion onto low-mass pre-main sequence (PMS) stars is no longer considered an oddity. It is now considered as one of the important stages in the grand scheme of evolution of the low-mass PMS stars, even though it is a poorly understood phenomenon. The short outburst timescales compared to the millions of years spent in the formation stage of these PMS stars make these events extremely rare, although statistically each PMS star is expected to experience ∼50 such short-duration outbursts during its formation stages (Scholz et al. 2013). The outburst durations, although short in timescale, are capable of delivering a substantial fraction of circumstellar mass onto the central PMS star (Vorobyov & Basu 2006). These events have been observed to span the entire age range of young stars starting from the embedded Class 0 sources to the Class II sources (Safron et al. 2015). Based on the outburst timescales and spectroscopic features, these classes of sources have been classically divided into two categories: (1) FUors, which experience a luminosity outburst of 4–5 mag that last for several decades and contain only absorption lines in their spectra, and (2) EXors experiencing a luminosity outburst of 2–3 mag, which last for a timescale of a few months to a few years and contains emission lines in their spectra (Herbig 1977; Hartmann & Kenyon 1996; Hartmann 1998). The physical origin of the sudden enhancement of accretion rate is not yet clear. However, a variety of models ranging from thermal instability, magneto-rotational instability, combination of magneto-rotational instability and gravitational instability, disk fragmentation to external perturbations have been proposed (Audard et al. 2014, pp. 387–410). To arrive at a general consensus about the physics behind such sudden enhancement of accretion rates, a large sample of FUor/EXor sources is required to test the above instability models. However, only about 25 FUor/EXor sources have been discovered so far (Audard et al. 2014, pp. 387–410). Therefore, any newly discovered source provides an important test-bed to probe the various physical aspects of episodic accretion and their comparison with the previous sources.

[15] NASA Earth and Space Science Fellow

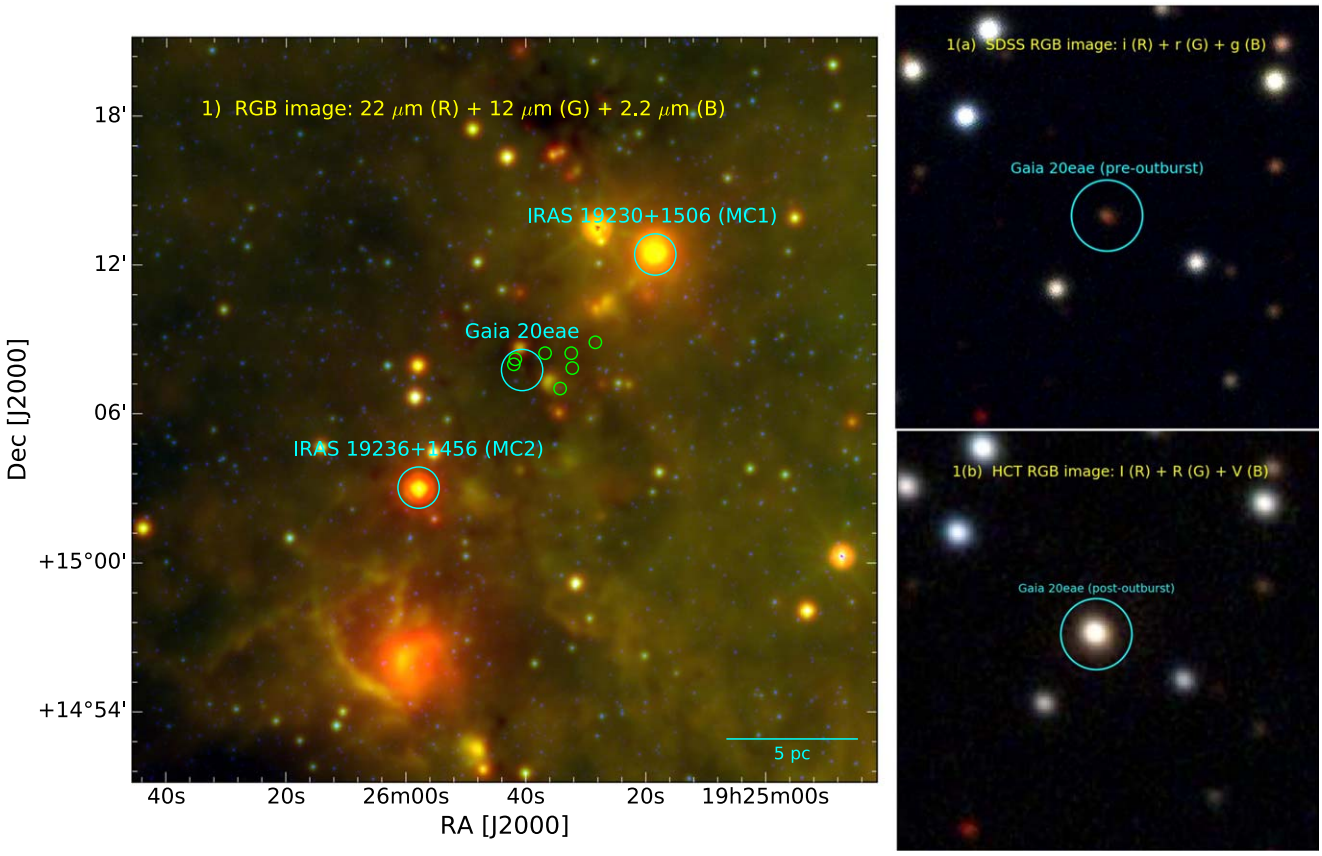

Figure 1. Color-composite image obtained by using the WISE 22 μm (red), WISE 12 μm (green), and 2MASS 2.2 μm (blue) images of the $\sim 30' \times 30'$ field of view around Gaia 20eae. The locations of Gaia 20eae, IRAS 19230 + 1506, and IRAS 19236 + 1456 (Retes-Romero et al. 2017) are shown by cyan circles. Locations of standard stars from the Zwicky Transient Facility (ZTF) sky survey are also shown with green circles. Subpanels 1(a) and 1(b) show the pre-outburst and post-outburst phases of Gaia 20eae in optical color-composite images taken from Sloan Digital Sky Survey (SDSS) and Himalayan Chandra Telescope (HCT), respectively.

The Gaia Photometric Alert System (Wyrzykowski et al. 2012; Hodgkin et al. 2013) is dedicated toward issuing transient alerts. Previously, it had issued three proven alerts for the eruptive young stars: Gaia 17bpi (Hillenbrand et al. 2018), Gaia 19ajj (Hillenbrand et al. 2019), and Gaia 18dvy (Szegedi-Elek et al. 2020). Among these, Gaia 17bpi and Gaia 18dvy are classified as FUors while Gaia 19ajj has been classified as an EXor, with its spectral features similar to that of V2492 Cyg (Hillenbrand et al. 2019). The Gaia alert system issued a notification on 2020 August 28 about Gaia 20eae with a transient identification number of AT2020nrs stating that it had undergone a 4.6 magnitude outburst. Prior to the Gaia alert, an alert for the same source was also generated by the Palomar Gattini-IR survey by Hankins et al. (2020). The rise timescales and the amplitude of the outburst suggest that this should be an FUor/EXor phenomenon. We have carried out optical and near-infrared (NIR) photometric and spectroscopic observations and combined them with the archival optical and infrared (IR) data to identify the outburst features of Gaia 20eae. In this paper, we present the initial findings of this source. Section 2 provides details on the location and distance of Gaia 20eae. Section 3 describes the observations and the data reduction procedures in detail. In Section 4 we describe the results obtained, and in Section 5 we conclude by providing our understanding of the present outburst in the context of the FUor/EXor phenomena.

2. Gaia 20eae: Location and Distance

The Gaia 20eae ($\alpha_{2000} = 19^{h}25^{m}40\overset{s}{.}61$, $\delta_{2000} = +15°07'46\overset{''}{.}5$; $| = 50\overset{°}{.}258492$, b $= -00.507730°$) is located near the edge of the W51 star-forming complex. The W51 star-forming region is known to be one of the most massive and active star-forming sites in our Galaxy, and is located at about 5 kpc from Earth (Ginsburg 2017). Retes-Romero et al. (2017) listed two molecular clouds, MC1 (size $\sim 15' \times 15'$) and MC2 (size $\sim 30' \times 36'$), in this direction at two different distances of 1.3 ± 0.2 kpc and 3.4 ± 0.4 kpc, respectively. The distances to these molecular clouds are derived kinematically using the CS $(2 \rightarrow 1)$ line velocities (Faúndez et al. 2004). MC1 and MC2 are also associated with IRAS sources IRAS 19230 + 1506 and IRAS 19236 +1456, respectively (Retes-Romero et al. 2017). These molecular clouds do not have any optical nebula associated with them, indicating that the star formation activity has started recently. Also, the IRAS sources have ultra-compact H II region (UCHII) colors, indicating that these molecular clouds are high-mass star-forming regions. In Figure 1, we show the location of Gaia 20eae along with the IRAS sources in the IR color-composite image generated from the Wide-field Infrared Survey Explorer (WISE) 22 μm (red), WISE 12 μm (green), and Two Micron All Sky Survey (2MASS) 2.2 μm (blue) images. Heated dust grains (22 μm emission) can be seen at several places, including at the IRAS locations of sources. The warm dust toward the south of Gaia 20eae is surrounded by 12 μm emission, which covers the

Table 1
Log of Photometric and Spectroscopic Observations

Telescope/Instrument	Date	Julian Day	Filters/Grisms	Exposure (sec) × Number of Frames
2.0 m HCT HFOSC	2020 August 29	2459091	*Gr*7, *Gr*8	2100 × 1, 1800 × 1
2.0 m HCT HFOSC	2020 August 30	2459092	*Gr*7	2400 × 1
2.0 m HCT HFOSC	2020 August 31	2459093	*B*, *V*, *R*, *I*, *Gr*7	120 × 1,60 × 1,30 × 1,30 × 2, 2400 × 1
2.0 m HCT HFOSC	2020 September 1	2459094	*Gr*7, *Gr*8	2400 × 1, 2400 × 1
2.0 m HCT HFOSC	2020 September 7	2459100	*B*, *V*, *R*, *I*, *Gr*7, *Gr*8	120 × 2, 60 × 2, 30 × 2, 30 × 2, 2400 × 1, 1800 × 1
10.0 m HET HPF	2020 September 11	2459104	NIR Cross dispersed echelle	617.7 × 2
2.0 m HCT HFOSC	2020 September 12	2459105	*B*, *V*, *R*, *I*	120 × 2, 60 × 2, 30 × 2, 30 × 2
10.0 m HET LRS2	2020 September 12	2459105	Optical low resolution spectra	157.7 × 2
2.0 m HCT HFOSC	2020 September 14	2459107	*B*, *V*, *R*, *I*, *Gr*7, *Gr*8	180 × 4, 60 × 4, 30 × 3, 30 × 2,2700 × 1, 2700 × 1
1.3 m DFOT 2KCCD	2020 October 11	2459134	*V*, *R*, *I*	10 × 30, 10 × 12, 10 × 12
1.3 m DFOT 2KCCD	2020 October 12	2459135	*V*, *R*, *I*	10 × 20, 10 × 8, 10 × 8
1.3 m DFOT 2KCCD	2020 October 13	2459136	*V*, *R*, *I*	15 × 20, 15 × 8, 15 × 8
0.5 m ARCSAT	2020 October 12	2459135	*g*, *r*, *i*, *z*	300 × 1,120 × 6,120 × 6,180 × 6
0.5 m ARCSAT	2020 October 13	2459136	*g*, *r*, *i*, *z*	360 × 5,300 × 5,240 × 11,240 × 5
0.5 m ARCSAT	2020 October 18	2459141	*g*, *r*, *i*, *z*	900 × 2,300 × 3,240 × 3
1.3 m DFOT 2KCCD	2020 October 19	2459142	*B*, *V*, *R*, *I*	60 × 4, 60 × 3, 60 × 1, 60 × 1
1.3 m DFOT 2KCCD	2020 October 20	2459143	*B*, *V*, *R*, *I*	60 × 4, 60 × 3, 60 × 1, 60 × 1
3.6 m DOT TANSPEC	2020 October 21	2459144	*J*, *H*, *K*	10 × 4 × 5 dither
3.6 m DOT TANSPEC	2020 October 24	2459147	Cross Dispersed spectra	150 × 8
3.6 m DOT TANSPEC	2020 November 6	2459160	Cross Dispersed spectra	150 × 8
1.3 m DFOT 2KCCD	2020 November 8	2459162	*B*, *V*, *R*, *I*	240 × 2, 150 × 1, 60 × 1, 60 × 1
1.3 m DFOT 2KCCD	2020 November 13	2459167	*B*, *V*, *R*, *I*	240 × 7, 150 × 7, 60 × 7, 60 × 7
1.3 m DFOT 2KCCD	2020 November 14	2459168	*B*, *V*, *R*, *I*	240 × 4, 150 × 2, 60 × 1, 60 × 1
1.3 m DFOT 2KCCD	2020 December 07	2459191	*V*, *R*, *I*	60 × 3,60 × 3,60 × 3

prominent polycyclic aromatic hydrocarbon features at 11.3 μm, indicative of a photon dominant region under the influence of feedback from massive stars (see, e.g., Peeters et al. 2004). This indicates that the Gaia 20eae is located at a site showing signatures of recent star formation activities. Until the release of data from the Gaia mission[16], there was no direct measurement of distance of the Gaia 20eae. Recently, adding corrections to the Gaia data release 3 (DR3) parallax by using the Bayesian inference approach to account for the nonlinearity of the transformation and the asymmetry of the resulting probability distribution, Bailer-Jones et al. (2021) estimated the distances of stars in our Galaxy. Therefore, for Gaia 20eae, we have adopted a distance of 3.2 ± 1 kpc as estimated by Bailer-Jones et al. (2021). As the molecular cloud MC2 is located in the same direction at a distance of 3.4 ± 0.4 kpc (Retes-Romero et al. 2017), Gaia 20eae seems to be associated with MC2. This makes it the farthest discovered FUor/EXor-type source until date. Almost all of the previously discovered FUors/EXors are located at a distance of ~1 kpc or less.

3. Observation and Data Reduction

3.1. Photometric Data

3.1.1. Present Data

We have monitored Gaia 20eae photometrically in optical bands at 16 different epochs with the Himalayan Faint Optical Spectrograph Camera[17] (HFOSC, four epochs) on the 2 m Himalayan Chandra Telescope (HCT), Hanle, India, ANDOR 2K CCD (nine epochs) on 1.3 m Devasthal Fast Optical Telescope (DFOT), Nainital India, and FlareCam 1K CCD[18] on 0.5 m Astrophysical Research Consortium (ARC) Small Aperture Telescope (ARCSAT; three epochs), New Mexico[19] from 2020 August to December. We have also obtained NIR photometric data of Gaia 20eae during its outburst state using the TIFR-ARIES Near Infrared Spectrometer (TANSPEC; Ojha et al. 2018) mounted on the 3.6 m Devasthal Optical Telescope (DOT), Nainital, India on the night of 2020 October 24. Table 1 provides the complete log of photometric observations presented in this work.

We have used standard data reduction procedures for the image cleaning, photometry, and astrometry (for details, see Sharma et al. 2020). We have derived the following color transformation equations using the available magnitudes in different filters (i.e., APASS DR10 archive[20] or 2MASS archive[21]) of all of the stars in the frame at epoch JD = 2459141 (for optical) and JD = 2459144 (for NIR).

$$B - V = 1.06 \pm 0.02 \times (b - v) - 0.71 \pm 0.03 \quad (1)$$

$$V - R = 0.77 \pm 0.02 \times (v - r) - 0.21 \pm 0.02 \quad (2)$$

$$R - I = 0.88 \pm 0.04 \times (r - i) + 0.66 \pm 0.02 \quad (3)$$

$$R - r = 0.09 \pm 0.04 \times (V - R) + 2.35 \pm 0.02 \quad (4)$$

$$J - H = 0.90 \pm 0.06 \times (j - h) + 0.05 \pm 0.09 \quad (5)$$

$$H - K = 1.00 \pm 0.07 \times (h - k) + 0.52 \pm 0.05 \quad (6)$$

$$J - j = 0.01 \pm 0.04 \times (J - H) - 1.20 \pm 0.04 \quad (7)$$

In order to calibrate the photometry of Gaia 20eae at other epochs, we have used these equations with intercept estimated from a set of seven non-variable standard stars (see Table 2).

[16] https://sci.esa.int/web/gaia
[17] https://www.iiap.res.in/iao/hfosc_details.html
[18] https://www.apo.nmsu.edu/Telescopes/ARCSAT/Instruments/arcsat_instruments.html
[19] Apache Point Observatory located in sunspot, New Mexico, which is operated by the Astrophysical Research Consortium (ARC). ARCSAT is a 0.5 m Classical Cassegranian Telescope, formerly known as the SDSS Photometric Telescope (PT).
[20] https://www.aavso.org/download-apass-data
[21] https://irsa.ipac.caltech.edu/Missions/2mass.html

Table 2
Coordinates of the Local Standard Stars

ID	α_{2000} (degrees)	δ_{2000} (degrees)	$zr \pm \sigma$ (mag)
1	291.423929	+15.136802	15.51 ± 0.01
2	291.424941	+15.133386	16.01 ± 0.01
3	291.403179	+15.140891	15.50 ± 0.01
4	291.384237	+15.130902	14.95 ± 0.01
5	291.384966	+15.140891	15.02 ± 0.01
6	291.392691	+15.117122	12.75 ± 0.01
7	291.368150	+15.148200	13.10 ± 0.01

These non-variable standard stars were identified from the Zwicky Transient Facility (ZTF) sky survey (Bellm et al. 2018) based on their zr-band light curves (LCs[22]). Table 3 lists the magnitudes of Gaia 20eae in different filters in different epochs of our observations.

3.1.2. Archival Data

We have also obtained the photometric data from the time domain Gaia sky survey (Gaia Collaboration et al. 2016, 2018). The Gaia sky survey maps the sky in the *G* band to look out for the transients and regularly updates on their Gaia Alert Index website.[23] We have obtained the *G*-band photometric data provided by the Gaia survey at its data archive.[24]

We have also acquired the pre-outburst *g*-, *r*-, *i*-, and *z*-band archival data from the Panoramic Survey Telescope and Rapid Response System (Pan-STARRS; PS1). Details about the PS1 surveys and latest data products are given in Chambers et al. (2016). We have downloaded the point-source catalog from the data release 2 of the PS1.[25]

Gaia 20eae was observed by the ZTF sky survey (Bellm et al. 2018). We obtained the archival *zr*-band photometric data of ZTF available from the NASA/IPAC Infrared Science Archive.[26] We also obtained recent photometric data in the *zg* and *zr* bands of the observation made by the ZTF survey from Lasair 2.0,[27] a community broker service to access, visualize, and extract science data.

We obtained the pre-outburst mid-infrared (MIR) magnitudes of Gaia 20eae from the Spitzer archive[28] in the 3.6, 4.5, 5.8, 8.0, and 24.0 μm wave bands. Pre-outburst magnitudes of Gaia 20eae are also obtained from the WISE archive[29] in the 3.4, 4.6, 12, and 22 μm wave bands. Outburst magnitudes of Gaia 20eae are obtained from the WISE/NEOWISE survey[30] in the 3.4 and 4.6 μm wave bands.

3.2. Spectroscopic Data

3.2.1. Medium-resolution Optical/NIR Spectroscopy

A photometric alert was issued by the Gaia alert system named AT2020nrs on 2020 August 28, 1:28 p.m. UTC. We immediately followed it using a medium-resolution ($R \sim 2000$) spectrograph "HFOSC" mounted on the 2 m HCT starting from 2020 August 29 itself. Using the *Gr*7 and *Gr*8 grisms of HFOSC, our spectroscopic observations spanned the optical wavelength range from ~4000 Å to 9000 Å. We have also observed the flux calibrator "Feige 110" on each night after Gaia 20eae to flux calibrate our HFOSC spectra. On 2020 September 12, we also obtained a medium-resolution optical spectrum ($R \sim 1140$, 1760, and 1920 for the orange arm, red arm, and far red arm, respectively) using the LRS-2 Red Integral Field Unit spectrograph on 10 m Hobby–Eberly Telescope (HET; Ramsey et al. 1998; Shetrone et al. 2007), USA. The LRS2-R spectrum was reduced using the standard LRS2 pipeline, Panacea.[31] Finally, we scaled our flux-calibrated spectra to match the flux and slope obtained from the photometric flux values of the same date. In case photometric magnitudes are not available on the same date, we have scaled our spectra with the photometric flux values of the nearest date. This is done to correct for any residual systematics in the flux calibration for the HFOSC due to its sensitivity to seeing variations and centering errors on the slit. This is also important for the LRS2 IFU observation, since the night was hazy due to smoke from wildfires, resulting in a highly variable non-gray atmospheric extinction.

We obtained NIR spectra of Gaia 20eae using the TANSPEC with its 0.″5 slit providing an $R \sim 2700$ on the nights of 2020 October 24 and 2020 November 6. Standard NIR dithering technique, i.e., obtaining the spectra at two different slit positions, was followed. The final spectrum of the object is obtained by subtracting the spectra obtained at the dithered positions to cancel the sky contribution. A telluric standard star was also observed immediately after the Gaia 20eae observations to remove the telluric features.

We have used the standard tasks of IRAF[32] to reduce medium-resolution spectroscopic data. The task APALL was used to extract the 1D spectrum. The extracted spectrum was then calibrated using the IDENTIFY task with the help of the calibration lamps taken immediately after the source spectrum. Finally, the CONTINUUM task of IRAF is used to continuum normalize the spectra in order to measure the equivalent widths (EWs) of different lines. The standard IRAF tasks STANDARD, SENSFUNC, and CALIBRATE were used to flux calibrate our spectra.

3.2.2. High-resolution Near Infrared Spectroscopy

We observed a high-resolution NIR spectrum of Gaia 20eae on 2020 September 12 using the Habitable Zone Planet Finder (HPF; Mahadevan et al. 2012, 2014) on the 10 m HET. HPF covers the wavelength range of 8100–12800 Å, at a spectral resolution of $R \sim 55{,}000$. The H2RG up-the-ramp raw data cube was reduced to 1D spectra by the procedures described in Ninan et al. (2018), Kaplan et al. (2019), and Stefansson et al. (2020). The wavelength calibration was done using a laser frequency comb calibrator as described in Metcalf et al. (2019). Barycentric correction was applied to all spectra with the values calculated using `barycorrpy` (Kanodia & Wright 2018).

[22] https://irsa.ipac.caltech.edu/Missions/ztf.html
[23] http://gsaweb.ast.cam.ac.uk/alerts/alertsindex
[24] https://gea.esac.esa.int/archive/
[25] http://catalogs.mast.stsci.edu/
[26] https://www.ipac.caltech.edu
[27] https://lasair.roe.ac.uk/
[28] https://irsa.ipac.caltech.edu/Missions/spitzer.html
[29] https://irsa.ipac.caltech.edu/Missions/wise.html
[30] https://irsa.ipac.caltech.edu/Missions/wise.html
[31] https://github.com/grzeimann/Panacea/blob/master/README_v0.1.md
[32] IRAF is distributed by National Optical Astronomy Observatories, USA, which is operated by the Association of Universities for Research in Astronomy, Inc., under cooperative agreement with National Science Foundation for performing image processing.

Table 3
Photometric Magnitudes of Gaia 20eae in Different Filters Using the Present Observations

JD	B (mag)	V (mag)	R_c (mag)	I_c (mag)	g (mag)	r (mag)	i (mag)	z (mag)	J (mag)	H (mag)	K_s (mag)
2459093	18.60 ± 0.03	16.49 ± 0.01	15.23 ± 0.01	14.33 ± 0.01	⋯	⋯	⋯	⋯	⋯	⋯	⋯
2459100	18.88 ± 0.01	16.74 ± 0.01	15.41 ± 0.01	14.45 ± 0.01	⋯	⋯	⋯	⋯	⋯	⋯	⋯
2459105	18.63 ± 0.01	16.52 ± 0.01	15.23 ± 0.01	14.38 ± 0.01	⋯	⋯	⋯	⋯	⋯	⋯	⋯
2459107	18.16 ± 0.01	16.47 ± 0.01	15.20 ± 0.01	14.27 ± 0.01	⋯	⋯	⋯	⋯	⋯	⋯	⋯
2459134	⋯	17.43 ± 0.01	16.11 ± 0.01	14.71 ± 0.02	⋯	⋯	⋯	⋯	⋯	⋯	⋯
2459135	⋯	17.19 ± 0.01	15.52 ± 0.01	14.66 ± 0.02	18.01 ± 0.07	16.24 ± 0.01	15.02 ± 0.01	14.22 ± 0.02	⋯	⋯	⋯
2459136	⋯	17.47 ± 0.02	15.68 ± 0.01	14.70 ± 0.01	17.94 ± 0.03	16.17 ± 0.04	15.03 ± 0.02	14.23 ± 0.02	⋯	⋯	⋯
2459141	⋯	⋯	⋯	⋯	17.86 ± 0.04	16.26 ± 0.07	15.11 ± 0.04	⋯	⋯	⋯	⋯
2459142	19.21 ± 0.03	17.38 ± 0.01	16.08 ± 0.01	14.72 ± 0.01	⋯	⋯	⋯	⋯	⋯	⋯	⋯
2459143	19.12 ± 0.04	17.14 ± 0.01	15.91 ± 0.02	14.61 ± 0.01	⋯	⋯	⋯	⋯	⋯	⋯	⋯
2459144	⋯	⋯	⋯	⋯	⋯	⋯	⋯	⋯	12.41 ± 0.02	11.27 ± 0.03	10.40 ± 0.03
2459162	19.54 ± 0.03	17.74 ± 0.01	16.41 ± 0.01	15.08 ± 0.01	⋯	⋯	⋯	⋯	⋯	⋯	⋯
2459167	18.67 ± 0.01	16.96 ± 0.01	15.73 ± 0.01	14.45 ± 0.01	⋯	⋯	⋯	⋯	⋯	⋯	⋯
2459168	18.77 ± 0.03	17.08 ± 0.01	15.83 ± 0.01	14.54 ± 0.01	⋯	⋯	⋯	⋯	⋯	⋯	⋯
2459191	⋯	17.52 ± 0.01	16.20 ± 0.01	14.89 ± 0.01	⋯	⋯	⋯	⋯	⋯	⋯	⋯

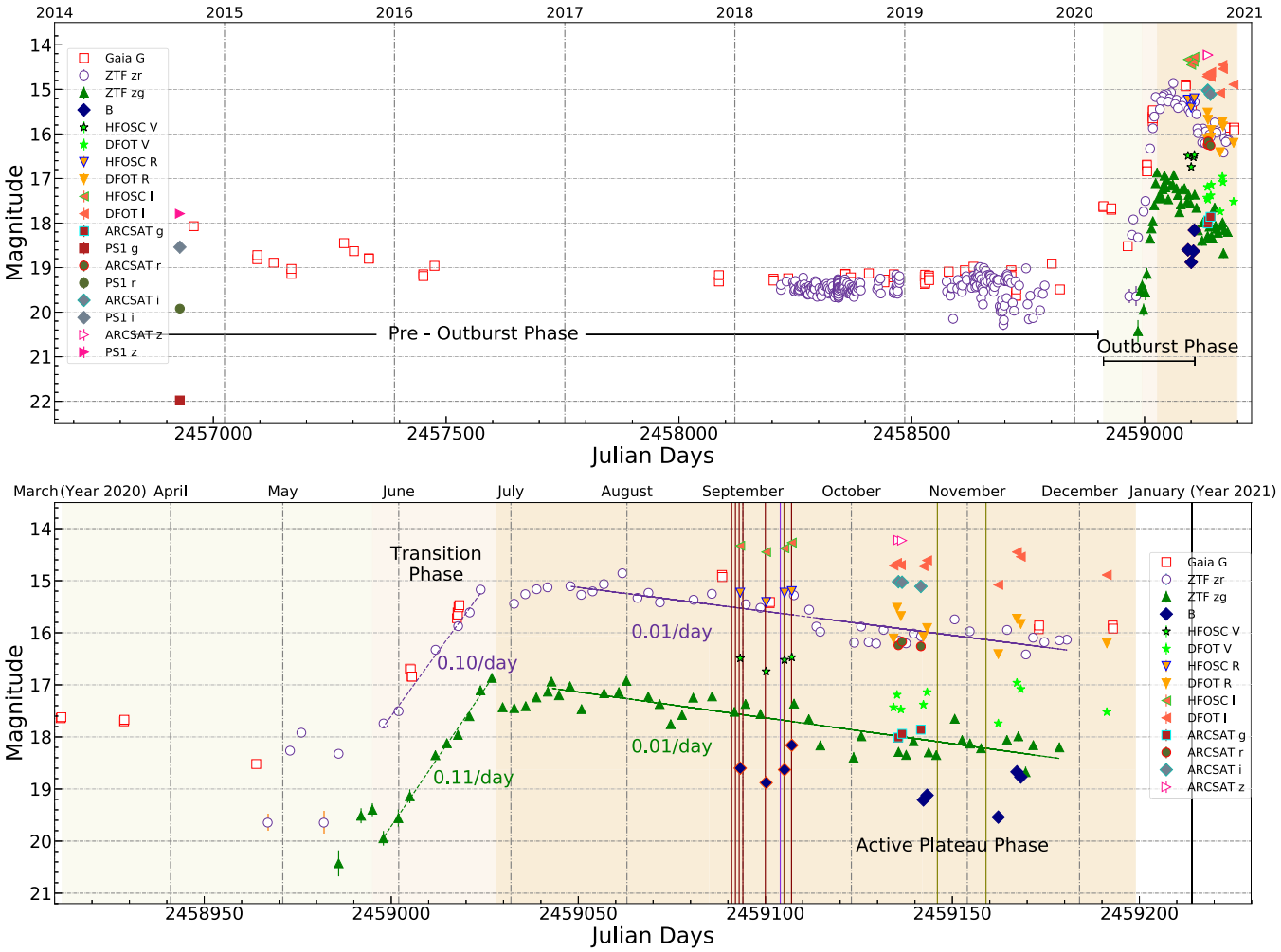

Figure 2. Upper panel: historical LC of Gaia 20eae in Gaia G, ZTF zg and zr, Johnson–Cousins B, V, R, and I_C and SDSS g, r, i, and z bands showing both pre-outburst (white region) and outburst (shaded region) phases. Lower panel: zoomed-in LC of Gaia 20eae in the outburst phase. The dark and intermediate brown regions represent the current plateau phase and the transition region, respectively. The vertical brown and magenta solid lines represent the epochs when HCT HFOSC and HET HPF spectra were taken, respectively. The olive line denotes the epoch of TANSPEC spectroscopic observations.

In summary, we have monitored Gaia 20eae spectroscopically at 10 different epochs with the HFOSC (6), TANSPEC (2), LRS2-R (1), and HPF (1). Table 1 provides the complete log of spectroscopic observations presented in this work.

4. Results and Analysis

4.1. Gaia 20eae during Quiescent Phase

4.1.1. Physical Properties

Gaia 20eae is named "SSTGLMC G050.2584-00.5077" and classified as a candidate young stellar object (YSO) due to its red color in MIR bands using the Spitzer photometry by Robitaille et al. (2008). Later on, this source was classified as a Class II YSO based on its IR spectral index (MC1-M15 in the Table 4 of Retes-Romero et al. 2017). Retes-Romero et al. (2017) also derived its mass as 1.5 $M_{\odot}$ assuming an age of 2 Myr for a typical Class II source and a distance of 1.3 kpc. As Bailer-Jones et al. (2021) have estimated a distance of 3.2 kpc for Gaia 20eae from Gaia DR3, this would result in a different mass estimation. However, in the absence of direct measurement of A_V around this source, it would be very difficult to derive its accurate physical parameters (e.g., age/mass).

4.1.2. Light Curve

The upper panel of Figure 2 shows the light curve (LC) of Gaia 20eae in Gaia G, ZTF zg and zr, Johnson–Cousins B, V, R, and I, and Sloan Digital Sky Survey (SDSS) g, r, i, and z bands. It is worthwhile to mention here that, although the ZTF (Bellm et al. 2018) and SDSS filters cover similar wavelengths, they have differences in their cutoff wavelength and transmission curve. The Gaia G-band data cover the longest time span of the LC starting from 2014 October 27 (JD = 2456957) to 2020 December 9 (JD = 2459192). The ZTF zr band has data from 2018 April 9 (JD = 2458218) to 2020 November 27 (JD = 2459180), whereas zg-band data are available from 2020 May 16 (JD = 2458985) to 2020 November 25 (JD = 2459178). The ZTF photometric data have better temporal sampling (2–3 days) as compared to the Gaia G-band data (10–15 days). The LC clearly demonstrates a long quiescent period with minor fluctuations until 2019 October 28 (JD = 2458785); after that, it began to transit to the present outburst stage. The pre-outburst magnitudes of Gaia 20eae were $G \sim 19.49$ mag (2019 November 30; JD = 2458818) and $zr \sim 19.40$ mag (on 2019 October 28; JD = 2458785). The mean G and zr magnitudes of Gaia 20eae during the quiescent phase were 19.14 ± 0.26 mag (from 2014 October 27 to 2019 November

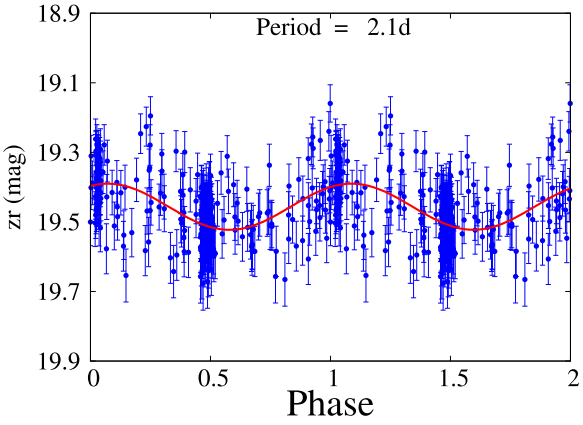

Figure 3. Quiescent phase folded LC of Gaia 20eae as obtained from the ZTF *zr*-band data. The period is determined by using the Period software and also cross-matched with the NASA Exoplanet Archive Periodogram service.

30) and 19.46 ± 0.17 mag (from 2018 April 9 to 2019 October 28), respectively.

As the quiescent phase LC of Gaia 20eae shows small-scale fluctuations, we searched for periodic variability in it using the ZTF *zr*-band data. Periodic variability has been reported in the PMS stars, which is due to the rotation of the star having hot and cool spots on its photosphere. We have used the Period[33] software, which works upon the principle of Lomb-Scargle (LS) periodogram (Lomb 1976; Scargle 1982), to determine the period of Gaia 20eae and to phase fold the LC. The advantage of the LS method is that it is effective even in case of the data set being non-uniformly sampled. We have also used the NASA Exoplanet Archive Periodogram[34] service for cross verification. The periods obtained in both the cases matched well. The period of Gaia 20eae thus comes out to be 2.1 ± 0.004 days. The period detected in the quiescent LC of the Gaia 20eae might correspond to the rotational period of the star. This type of period is commonly observed in Class II/III type of YSOs as shown by Sinha et al. (2020). Figure 3 shows the phase folded LC of the Gaia 20eae during its quiescent phase. The amplitude of variation is of the order of 0.2 mag, which is also typical of Class II/III type of YSOs (Sinha et al. 2020).

4.2. Gaia 20eae during Outburst Phase

4.2.1. Light Curve

In the lower panel of Figure 2, we show the LC of Gaia 20eae in the *B*, *V*, *R*, *I*, *G*, *zg*, *zr*, *g*, *r*, *i*, and *z* bands in the outburst phase. The LC starts from 2020 March 3 (JD = 2458800) up to the latest data point on 2020 December 9 (JD = 2459192). The LC of Gaia 20eae is peculiar in the sense that the rise to peak brightness consists of two parts: an initial slow rise from the quiescent phase starting from JD = 2458800 to JD = 2458995 and then a rapid rise to the peak brightness from JD = 2459014 to JD = 2459047, reaching maximum brightness on JD = 2459047, and then a slowly decaying phase (JD = 2459047 to JD = 2459145). It also shows small-scale fluctuations with amplitude of ~0.2 mag on a timescale of a few days. We were not able to derive the periodicity of these fluctuations using the LS periodogram. We call the rapid rise part and the slowly decaying part of the LC "transition phase" and "active plateau phase," respectively; they are labeled and shadowed with different colors in the lower panel of Figure 2. We have calculated the rise rate and decay rate of Gaia 20eae in different wavelengths from the available Gaia and ZTF data by fitting a least-squares straight line in the different phases of the LC. The fits for the data points in the transition and active plateau phases are shown in the lower panel of Figure 2. The overall best-fit rise rate from the quiescent phase to the maximum brightness is calculated to be 0.6 mag/month in the *G* band, over a duration of ~247 days. This rise rate is prone to higher uncertainties as there are lots of data gaps in the LC initially. The rise rate in the transition phase was found to be similar, i.e., ~0.1 mag day^{-1} or ~3 mag month^{-1} in the *G*, *zg*, and *zr* bands. The decay rate in the active plateau phase is calculated as 0.01 mag day^{-1} (or 0.3 mag month^{-1}) for a duration of ~98 days, which is an order less than the rise rate. It is to be noted here that Gaia 20eae has not returned to its quiescent state. Hence, the decay rate that we calculated is obtained by considering the data range that we have presented in this study.

The maximum brightness in the current outburst phase in the *zg* and *zr* bands is recorded on 2020 July 16 (JD = 2459047) as 17.02 mag and 15.09 mag, respectively. In the *G* band, the source reached the maximum brightness of 14.89 magnitude on 2020 August 26 (JD = 2459088). Thus, the current outburst magnitude amplitudes are: $\Delta G = 4.25$ mag and $\Delta zr = 4.37$ mag.

The LCs in *B*, *V*, *R*, and *I* also follow the trend of the ZTF and Gaia LCs. The quiescent phase *J*, *H*, and K_s magnitudes of Gaia 20eae are 14.67 mag, 13.36 mag, and 12.16 mag, respectively, as obtained from the UKIDSS DR10plus. During the present outburst stage, the *J*, *H*, and K_s magnitudes of Gaia 20eae as obtained from TANSPEC are 12.41 mag, 11.27 mag, and 10.40 mag, respectively. This implies that the present outburst is similar to the FUor family of objects and is almost wavelength independent.

4.2.2. The Evolution of the Photometric Spectral Energy Distribution

Figure 4 (left panel) represents the spectral energy distributions (SEDs) of Gaia 20eae during its quiescent and active states represented by the red and cyan curves, respectively. We constructed the quiescent phase SED using the multiwavelength data (optical to MIR wavelengths, i.e., 0.44 (*B*), 0.55 (*V*), 0.65 (*R*), 0.80(*I*), 1.2 (*J*), 1.6 (*H*), 2.2 (K_s), 3.4(W1), 3.6(*I*1), 4.6(W2), 4.5(*I*2), 5.8(*I*3), 8.0(*I*4), 12(W3), 22(W4), and 24(*I*4) μm) taken from the data archives (PS1, 2MASS, Spitzer, and WISE). The PS1 magnitudes were transformed to Johnson–Cousins system by using the equations given by Tonry et al. (2012). For the outburst state SED, we have used current optical and NIR band observations as well as NEOWISE data. Apart from having a shift in the brightness, there is clearly a change in the shape of the SED at the longer wavelengths as compared to the shorter wavelengths. This change in the SED can be quantified by comparing the differences in observed magnitudes of Gaia 20eae with those of pure dust-clearing events. The right panel of Figure 4 shows the observed magnitude differences of Gaia 20eae between its quiescent and active state by a blue curve. We compare the magnitude variations against $\Delta A_z = -2$ mag and $\Delta A_z = -4$ mag for $R_V = 3.1$ and $R_V = 5.5$ dust laws (see also, McGehee et al. 2004). From the deviation of the observed magnitude difference with the dust-clearing events, we can conclude that the brightening of Gaia 20eae cannot be explained

[33] http://www.starlink.rl.ac.uk/docs/sun167.htx/sun167.html
[34] https://exoplanetarchive.ipac.caltech.edu/docs/tools.html

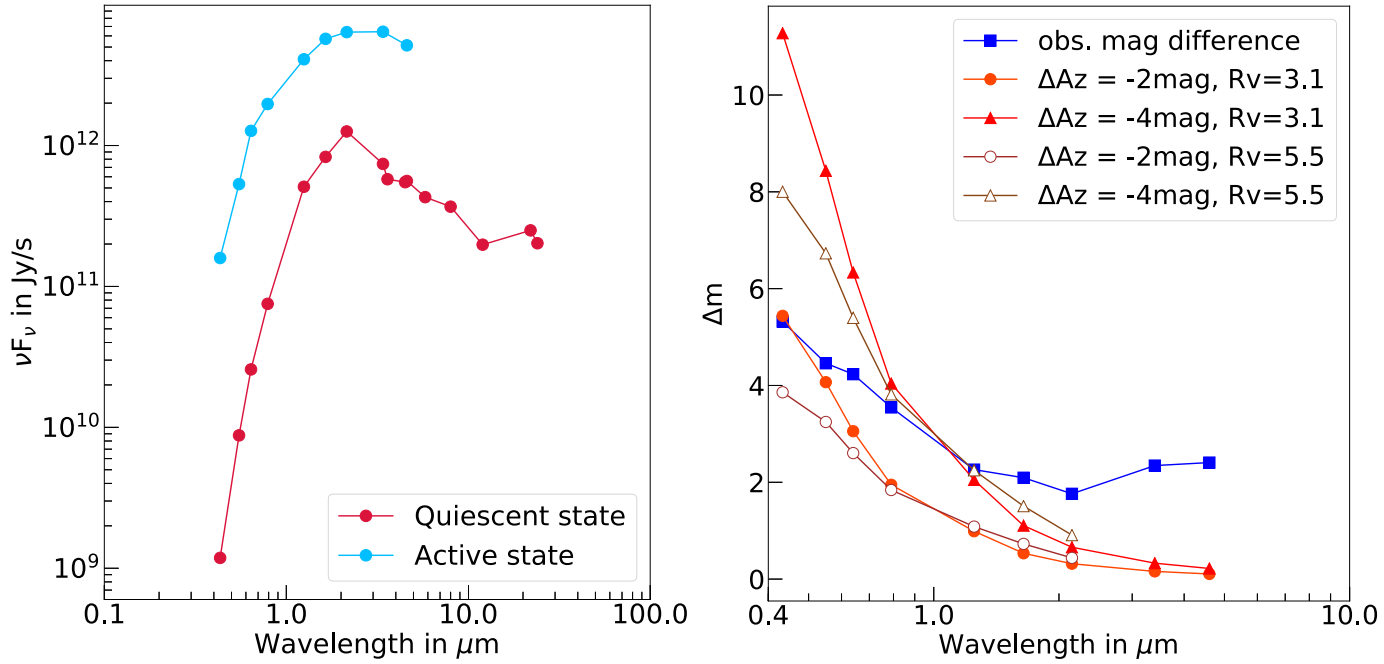

Figure 4. Left panel: the photometric SEDs of Gaia 20eae in the quiescent (red dots) and active (cyan dots) phases. Right panel: changes in SEDs, the observed magnitude differences (squares) are compared against pure dust-clearing events for $A_z = -2$ mag (circles) and $A_z = -4$ mag (triangles) and for $R_V = 3.1$ (filled) or $R_V = 5.5$ (open) dust laws.

Table 4
Reddening-invariant Colors in the Quiescent and the Outburst Phases of the Gaia 20eae

Days (JD)	$Q_{BVR} \pm \sigma$ (mag)	Nσ	$Q_{VRI} \pm \sigma$ (mag)	Nσ	Days (JD)	$Q_{BVR} \pm \sigma$ (mag)	Nσ	$Q_{VRI} \pm \sigma$ (mag)	Nσ
2456928	0.25 ± 0.15	⋯	0.00 ± 0.07	⋯	2459135	⋯	⋯	0.88 ± 0.02	−12.0
2459093	0.18 ± 0.04	0.5	0.42 ± 0.01	−5.9	2459141	-0.16 ± 0.04	2.7	0.03 ± 0.02	−0.5
2459100	0.10 ± 0.01	1.0	0.44 ± 0.01	−6.3	2459142	0.09 ± 0.05	1.0	0.02 ± 0.03	−0.3
2459105	0.14 ± 0.01	0.8	0.50 ± 0.01	−7.0	2459161	-0.24 ± 0.04	3.3	0.09 ± 0.02	−1.3
2459107	-0.25 ± 0.01	3.4	0.40 ± 0.01	−5.7	2459166	-0.17 ± 0.01	2.8	0.04 ± 0.01	−0.5
2459133	⋯	⋯	0.02 ± 0.02	−0.2	2459167	-0.22 ± 0.04	3.1	0.05 ± 0.01	−0.7
2459134	⋯	⋯	0.87 ± 0.02	−11.9	2459190	⋯	⋯	0.10 ± 0.01	−1.4

Note. Nσ is the ratio of color change to the quadrature sum of measurement errors.

by the diminishing of the line-of-sight extinction, rather the enhancement of accretion rate is the likely cause.

Using the multiepoch data from the PS1 archive (quiescent phase), 2 m HCT and 1.3 m DFOT (outburst phase), we have also examined the evolution of the reddening-invariant colors, "Q_{xyz}" of Gaia 20eae as it transitioned from quiescent state to the eruptive state. The reddening-invariant colors have a generic form of : $Q_{xyz} = (x - y) - [(y - z)E(x - y)/E(y - z)]$, where x, y, and z are the observed magnitudes in each passband (McGehee et al. 2004). A color change having $\Delta\ Q_{xyz} \neq 0$ indicates that the changes in SED are not due to pure dust clearing. The estimated reddening-invariant colors (for $R_V = 3.1$) for Gaia 20eae as it transitioned from the quiescent state to the active state are listed in Table 4. The large change in most of the Q_{xyz} values also points toward that the increase in the brightness of Gaia 20eae is not consistent with a dust-clearing event, rather an intrinsic change occurred in the SED. It is also to be noted that in the "active plateau region" of Gaia 20eae starting from JD = 2549141, the value of Q_{VRI} is close to 0. This might imply that there was no change in the SED intrinsically in this duration.

4.2.3. Spectral Features

Figure 5 shows our medium-resolution spectra covering a very broad wavelength range (∼0.4–2.4 μm). The optical spectra are flux-calibrated whereas the NIR spectra are only normalized spectra. Both the optical and NIR spectra of Gaia 20eae consist of a mixture of the lines typically observed in the FUor and EXor family of sources. Evolution of these spectral lines at different epochs of the outburst phase is shown in Figure 6. Similar to the FUor sources, Gaia 20eae exhibits blueshifted absorption features in the Na I resonance line and the Hβ line, indicative of the powerful winds from the source. It also shows a strong P Cygni profile in the Hα and Ca II IR triplets (IRT) in emission. The Fe II line at λ5018 Å, which is seen in emission in EX Lupi, is found to be in absorption, but the Fe II line at λ6433 Å is found to be in emission. K I λ7694 Å and O I λ8446 Å lines are found to be in absorption. The strength of Hβ and Na I D lines can be seen decreasing during the outburst phase of Gaia 20eae. Spectroscopically, in the optical regime, the spectrum of Gaia 20eae resembles a FUor, whereas in the NIR regime, it is more or less similar to an EXor.

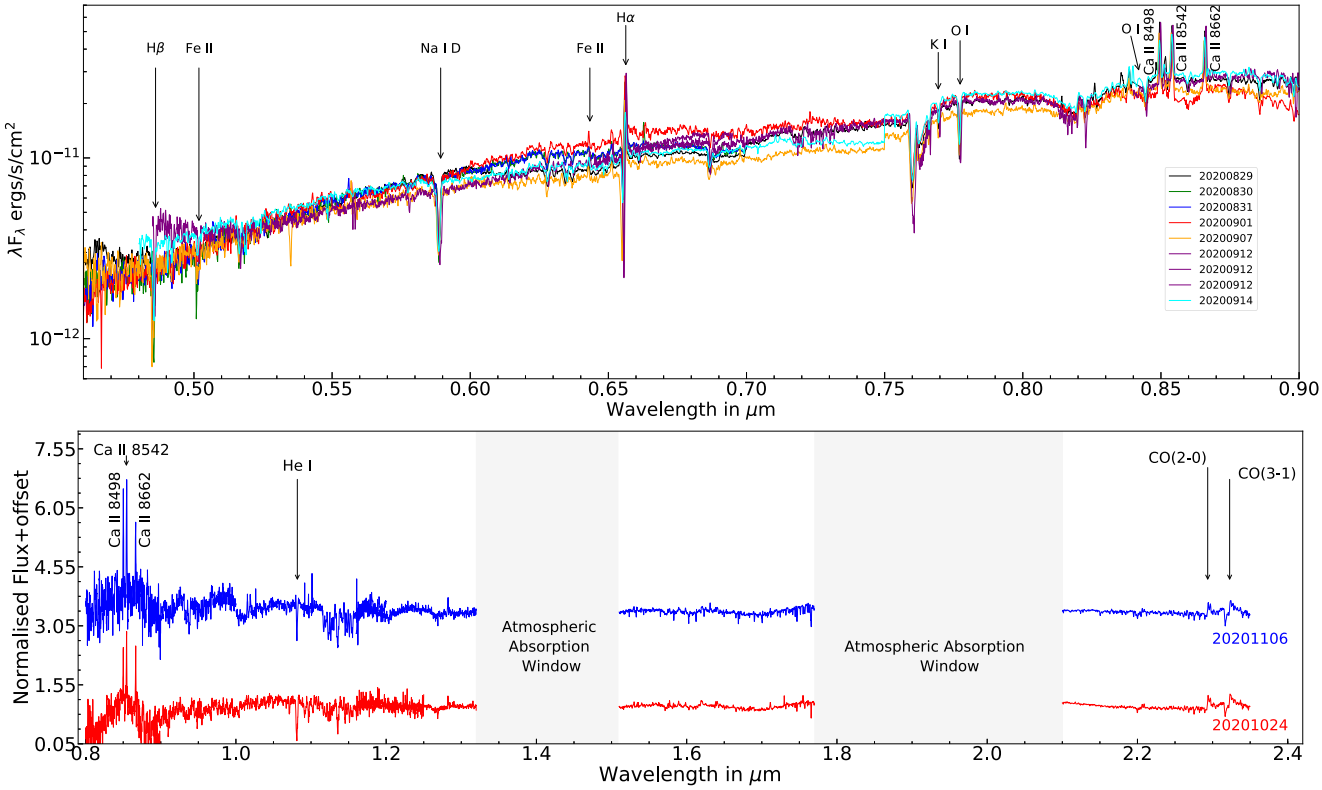

Figure 5. Evolution of the flux-calibrated spectra of Gaia 20eae during our monitoring period obtained using HFOSC on 2 m HCT and LRS2 on 10 m HET starting from 2020 August 29 to 2020 September 14 (upper panel). The lines used for the present study have been marked. The flux-calibrated spectrum shows variation in the continuum level that is also present in the LC. The lower panel shows the normalized flux of Gaia 20eae obtained using TANSPEC on 2020 October 24 and 2020 November 06.

Our medium-resolution NIR spectra show several distinct spectral features, most of them are in absorption. The gaps in the spectra represent atmospheric absorption windows due to the broad H_2O and OH bands. We could identify some prominent lines: Ca II IRT, He I at λ10830 Å, and the CO bandheads.

CO bandhead in K band. The CO (2-0) and CO(3-1) bandhead absorptions are one of the defining characteristics of FUors (Hartmann 1998). The CO bandheads in Gaia 20eae are in emission, implying a temperature inversion at the surface of the protoplanetary disk. This is similar to that observed in other EXor sources like V2492 Cyg (Aspin 2011). Thus based on the CO bandhead lines, Gaia 20eae resembles more of an EXor source.[35]

Radial velocity of Gaia *20eae.* Due to a lack of symmetric photospheric lines in the high-resolution spectrum of Gaia 20eae, it is hard to estimate the radial velocity of the star. The chromospheric Fe I emission lines were found to be the most symmetric lines in the spectrum, and the line center of the Fe λ8387.77 Å at 20 km s^{-1} is taken as the stellar radial velocity with respect to the solar system barycentre in this study. The corresponding velocity in the local standard of rest reference frame comes out to be ~35 km s^{-1}. It is to be mentioned that the peak velocity of the ^{13}CO for the molecular cloud "MC2" is 42 km s^{-1} with respect to the local standard of rest (Retes-Romero et al. 2017).

[35] It should be noted that some intermediate FUor/EXor sources like V1647 Ori have shown CO bands in both emission as well as in absorption at different stages of its outbursts.

4.3. Physical Parameters of Gaia 20eae during Outburst Phase

4.3.1. Disk Turbulence and Outflow Wind Velocities

Panel (d) in Figure 6 represents the evolution of the O I line at λ7773 Å of Gaia 20eae during our spectroscopic monitoring period. The formation of the O I line at λ7773 Å in T Tauri stars, which is an indicator of turbulence, is attributed to the presence of warm gas in the envelope surrounding the disk or in the hot photosphere above the disk (Hamann & Persson 1992a). Table 5 shows the variation in the value of the equivalent width (EW) of O I line at λ7773 Å during our monitoring period. The mean value of the equivalent width of O I line at λ7773 Å is estimated as 4.7 ± 1.2 Å. The scatter in the EW values is twice the error in its estimation, indicating the presence of a turbulent medium surrounding Gaia 20eae during its outburst phase. For future inference, we have also tabulated the EW values of other lines during different epochs of the outburst phase of Gaia 20eae in Table 5.

The outflow wind velocity of the Gaia 20eae is estimated from the blueshifted absorption minima of the Hα, Na I D, and Hβ lines (Hartmann 1998). The estimated values of wind velocity by Doppler shift at different epochs in the outburst phase of Gaia 20eae are listed in the Table 5. The values show the variation from -630 to -203 km s^{-1}. The mean velocity of the outflow wind velocity for Hα, Na I D, and Hβ comes out to be -505 ± 62 km s^{-1}, -356 ± 49 km s^{-1}, and -339 ± 136 km s^{-1}, respectively. The typical error in the outflow wind velocity estimation is ~25 km s^{-1}; therefore, a large scatter in its values can be attributed to intrinsic variation of outflow winds during the outburst phase.

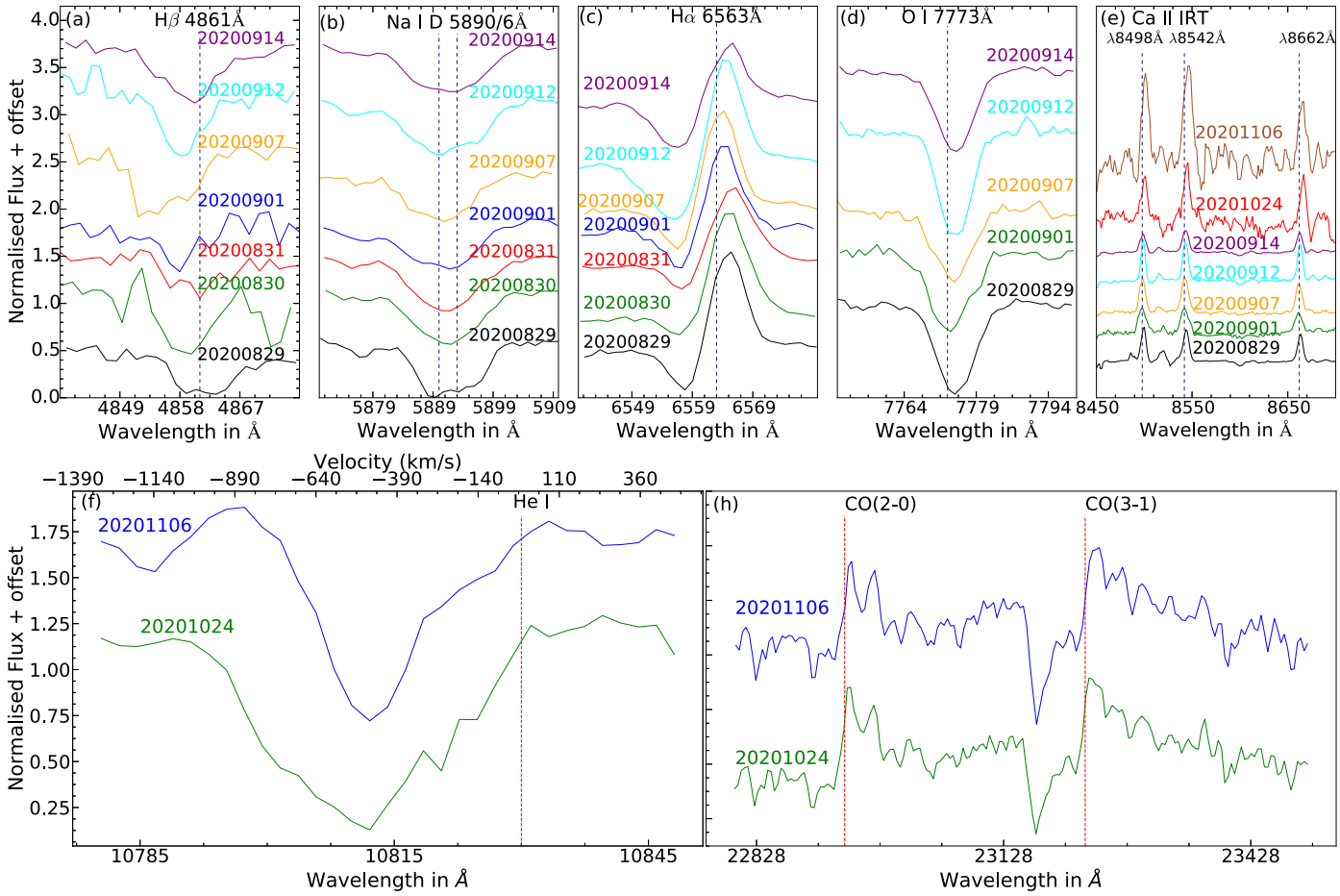

Figure 6. Evolution of the Hβ, Na I D λ5890/6 Å, Hα, O I λ7773 Å, Ca II IRT, He I, CO(2-0), and CO(3-1) lines during our monitoring period.

Resonant scattering from meta-stable helium atoms is an excellent tracer of the outflow winds from YSOs (Edwards et al. 2003). The EUV to X-ray radiation from magnetospheric accretion or chromosphere activity can cause significant formation of the meta-stable triplet ground state of helium atoms. During the ~2.5 hr when they typically survive in this meta-stable state, they could resonant scatter the λ10830 Å photons, resulting in a strong absorption signal at the local velocity of the gas. Figure 7 shows the very strong blueshifted He λ10830 Å absorption signature in the high-resolution spectrum of Gaia 20eae. On the red side, the absorption profile extends to about $+200\,\mathrm{km\,s^{-1}}$, and on the blue side, the absorption profile extends beyond $-400\,\mathrm{km\,s^{-1}}$. Unfortunately, the high-resolution spectrum beyond $-400\,\mathrm{km\,s^{-1}}$ could not be measured since it falls outside the detector in the HPF spectrograph. Our medium-resolution TANSPEC spectra in panel (f) in Figure 6 shows the blueshifted absorption extending to $-513\,\mathrm{km\,s^{-1}}$ on 2020 October 24 and reducing to $-493\,\mathrm{km\,s^{-1}}$ by 2020 November 6. Such strong blueshifted He λ10830 Å triplet signatures are common in YSOs with strong outflows. Gaia 20eae is not an exception. The reduction in the blueshifted wing velocity of He λ10830 Å over a span of two weeks could be either due to change in the structure of the outflow winds or due to drop in the EUV–X-ray irradiation.

4.4. Magnetospheric Accretion and Line Profiles

High-resolution line profile shapes provide us with direct measurement of the kinematics of the hot gaseous environment of the accretion region. In this section we highlight some of the most interesting line profiles we detected in Gaia 20eae.

4.4.1. Infall Signature in Ca II IRT

Ca II IR triplet emission lines are believed to originate in the active chromosphere as well as in the magnetospheric accretion funnel regions (Hamann & Persson 1992b; Muzerolle et al. 1998). Our observation of Gaia 20eae on 2020 September 12 detected a redshifted absorption component (with respect to the stellar rest frame) in all three Ca II IR triplet lines (See Figure 8). The smooth curves show the best fit of a double Gaussian model, where the first component fits the broad emission line, and the second component fits the redshifted absorption component at $+25\,\mathrm{km\,s^{-1}}$. The redshifted absorption cannot originate in stellar wind or outflows. One possible region of origin could be the hot infalling gas in the magnetospheric accretion funnel (Edwards et al. 1994). The lower panel in Figure 8 shows this absorption component normalized to the fitted emission line profile. The ratio of equivalent widths of these absorption components (EqW: 0.27, 0.49, 0.41 Å) is inconsistent with the optically thin line formation scenario (1:9:5).[36]

Constraint on the viewing angle. The detection of the absorption profile implies the line of sight is along the

[36] This is unlike the optically thin blueshifted absorption from winds typically seen in similar FUors/EXors V1647 Ori and V899 Mon (Ninan et al. 2013, 2015).

Table 5
Variations of the Wind Velocities as Obtained from Blueshifted Absorption Dips of Hα, Na I D, and Hβ and Equivalent Width (in Å) Variations of the Optical Lines in Gaia 20eae

Date	JD	Wind velocity (km s^{-1})			Equivalent Width (Å)						
		Hα	Na I D	Hβ	Hβ	Na I D	Hα	[O I] λ7773	Ca II λ8498	Ca II λ8542	Ca II λ8662
2020 Aug 29	2459091	−422	−303	−313	4.5 ± 0.3	4.8 ± 0.6	−5.1 ± 0.7	4.3 ± 0.6	−5.0 ± 0.6	−4.8 ± 0.6	−6.1 ± 0.6
2020 Aug 30	2459092	−513	−293	−203	7.2 ± 0.3	3.0 ± 0.3	−4.5 ± 0.6	⋯	⋯	⋯	⋯
2020 Aug 31	2459093	−512	−362	−200	4.1 ± 0.3	2.9 ± 0.3	−5.6 ± 0.7	⋯	⋯	⋯	⋯
2020 Sept 01	2459094	−451	−438	−301	5.4 ± 0.3	4.2 ± 0.5	−5.1 ± 0.7	4.5 ± 0.6	−6.7 ± 0.8	−7.2 ± 0.8	−6.5 ± 0.7
2020 Sept 07	2459100	−619	−384	−630	8.3 ± 1.8	6.6 ± 1.2	−8.3 ± 1.0	3.4 ± 0.6	−7.1 ± 0.9	−9.3 ± 1.0	−10.3 ± 0.9
2020 Sept 12	2549105	⋯	⋯	−320	4.8 ± 0.0	9.9 ± 0.0	−8.6 ± 0.0	4.6 ± 0.0	−6.4 ± 0.0	−7.8 ± 0.0	−6.6 ± 0.0
2020 Sept 14	2459107	−516	−356	−407	6.3 ± 1.1	8.7 ± 1.3	−5.6 ± 0.8	4.4 ± 0.7	−4.6 ± 0.6	−5.5 ± 0.7	−4.8 ± 0.6

Note. The error in the equivalent width is estimated using the relation provided by Cayrel (1988).

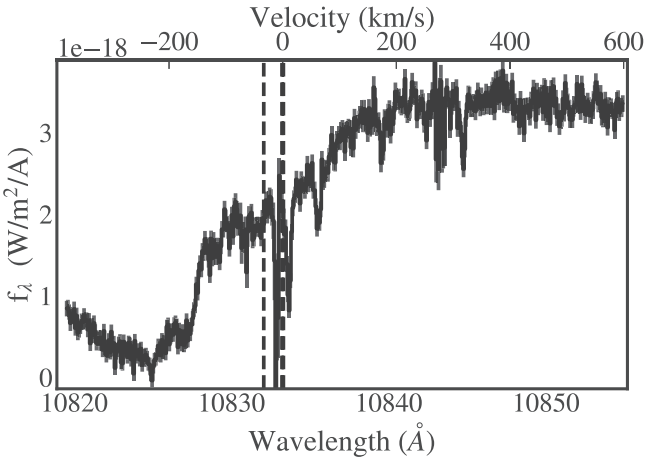

Figure 7. High-resolution line profile of the He 10830 triplet on 2020 September 12 showing a large blueshifted component, likely originating in the strong outflow from Gaia 20eae. The absorption signal extends from +200 km s^{-1} on the red side, to beyond −400 km s^{-1} on the blue side (the profile is truncated at the detector edge in HPF). The vertical dashed lines show the location of the He 10,830 triplets in the stellar rest frame. The narrow lines in the spectrum are telluric.

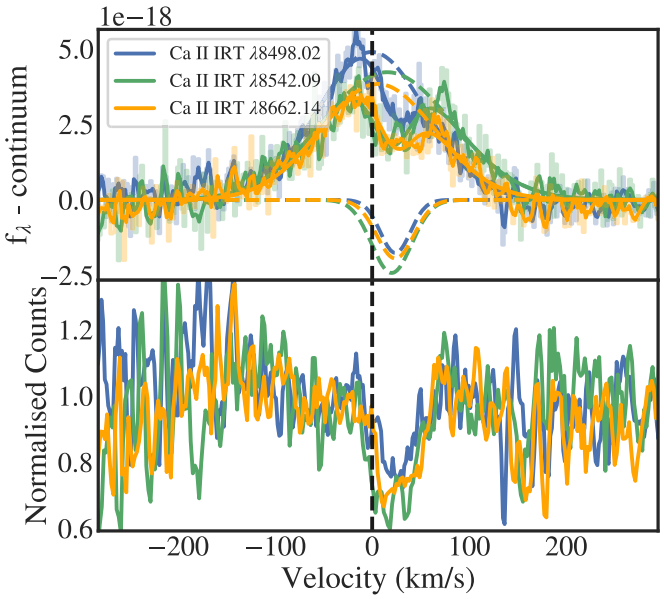

Figure 8. Top panel: high-resolution line profiles of all three Ca II IRT lines on 2020 September 12 showing a redshifted absorption component. This is likely originating in the magnetospheric accretion funnel. The fainter step style plots behind the bold lines are the measured spectra. The bold curves are a 3 pixel smoothed spectra shown for clarity. The thin smooth curve is the double Gaussian composite fit of the emission at the stellar rest velocity and a redshifted absorption at ∼+25 km s^{-1}. The individual components are shown in dashed curves. Lower panel: normalized spectrum using the continuum plus the fitted emission Gaussian component.

increasing temperature gradient, and we are not seeing an infalling hot gas in the foreground of a cooler environment, i.e., the viewing angle is through the accretion funnel to the footprint on the stellar surface where it is hottest. For a star of mass M, radius R_*, and disk infall radius r_m, the velocity of the infalling gas along the magnetic field line direction is given by the formula $v_p(r) = \left[\frac{2GM}{R_*}\left(\frac{R_*}{r} - \frac{R_*}{r_m}\right)\right]^{1/2}$ (Hartmann et al. 1994). For Gaia 20eae, this would imply a velocity of ∼350 km s^{-1} at the base of the funnel, of the order of ∼50 km s^{-1} (or ∼25 km s^{-1} along line of sight) at a radius very close to start of infall near the truncated accretion disk. This, combined with the requirement of a hotter background against which this low-velocity infall gas is viewed, constrains the viewing angle as shown in Figure 9.

4.4.2. Hydrogen Paschen Lines

Figure 10 shows the Hydrogen Paschen lines from Pa (14–3) to Pa γ (6–3). Only the lines that are not completely lost in telluric bands are plotted here. The higher energy level Paschen lines are detected as broad absorption lines extending from −250 km s^{-1} to +250 km s^{-1}. However, in the lowest energy levels lines, Paγ λ10938.086 and Paδ λ10049.369, on top of the broad absorption component, we also detect an emission component at the core of the lines. The strength of this emission component decreases as we go to lines of higher energy levels.

4.4.3. Fe I and Ti I Lines

We detect multiple Fe I and Ti I lines in emission from Gaia 20eae during its high accretion phase (Figure 11). These lines typically originate in the active chromosphere, and are relatively symmetric when not blended with other lines. Hence, the peak positions of these lines were used to measure the 20 km s^{-1}

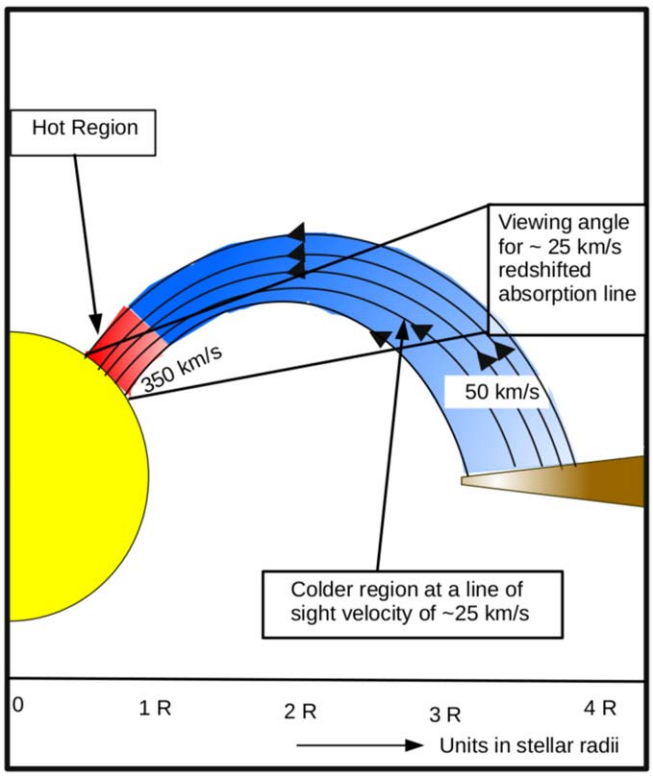

Figure 9. Diagram of the classical dipole magnetospheric accretion funnel, and the region of the viewing angles that could potentially result in a low-velocity redshifted absorption signature on top of the broad Ca II IR triplet emission line is shown in the diagram.

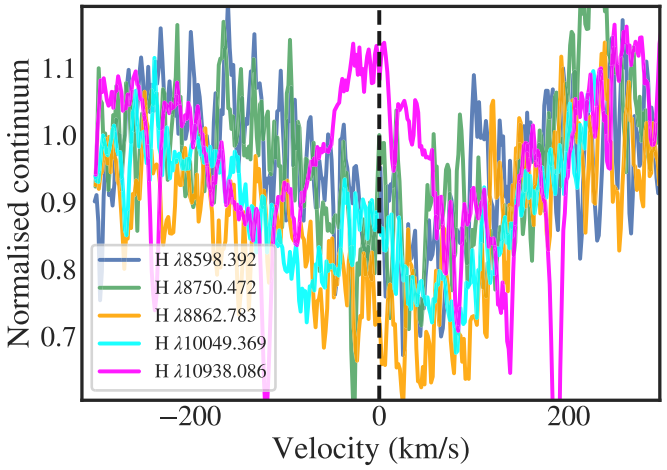

Figure 10. Hydrogen Paschen lines from Pa (14–3) to Pa γ (6–3). The lines that are completely lost in telluric bands are not plotted. The narrow lines in Paγ λ10938.086 are telluric. The higher energy Paschen lines are detected as broad absorption lines starting from -250 km s^{-1} to $+250$ km s^{-1}. We detect emission at the line core for the lower energy level lines Paγ λ10938.086 and Paδ λ10049.369 on top of the broad absorption component. The bold curves are a 3 pixel smoothed spectra shown for clarity.

radial velocity of Gaia 20eae. The widths of these emission lines are similar across the spectrum.

5. Discussion and Conclusions

Gaia 20eae is the farthest discovered FUor/EXor-type Class II YSO undergoing an outburst of $\sim$4.25 mag in the G band. We have found that the present brightening of Gaia

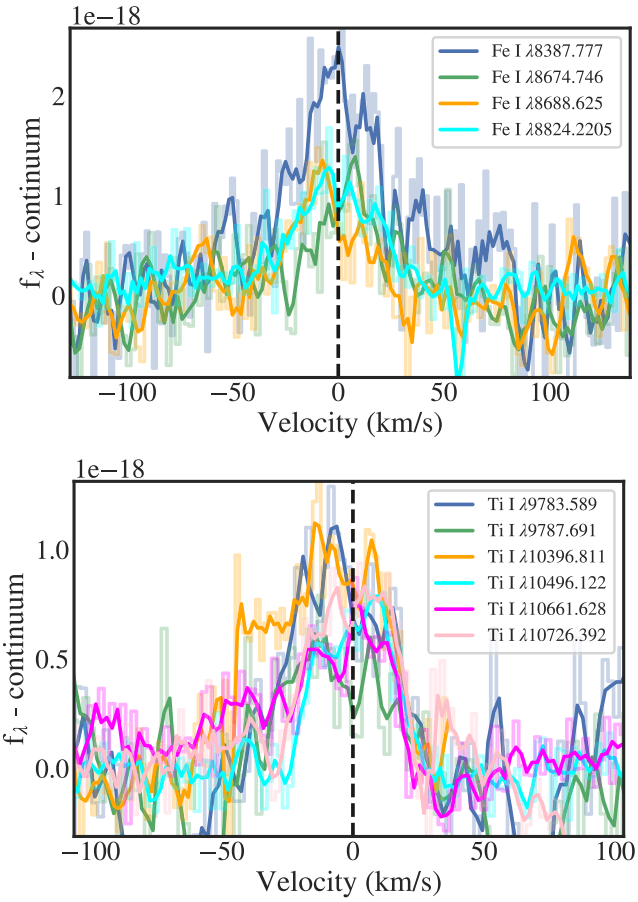

Figure 11. High-resolution line profiles of four Fe I lines and six Ti I emission lines on 2020 September 12. These lines are likely originating in the active chromosphere of Gaia 20eae. The fainter step style plots behind the bold lines are the measured spectra. The bold curves are a 3 pixel smoothed spectra shown for clarity.

20eae is not due to the dust clearing from our line of sight toward the source but due to an intrinsic change in the SED (warming of the continuum component). The LC of Gaia 20eae in the quiescent phase is showing a small-scale fluctuation of amplitude of 0.2 mag and period of $\sim$2 days.

In the outburst phase, Gaia 20eae is showing a transition stage during which most of its brightness ($\sim$3.4 mag) has occurred at a short timescale of 34 days with a rise rate of 3 mag month^{-1}. This rise rate of Gaia 20eae during the transition stage is greater than most of the recorded rise rates of the FUor/EXor family of sources during the outburst phase, e.g., V899 Mon (0.04–0.15 mag month^{-1}; Ninan et al. 2015), Gaia 18dvy (0.42 mag month^{-1} in the Gaia G band; Szegedi-Elek et al. 2020; a newly discovered FUor) and V1118 Ori (1.05 mag month^{-1}; Giannini et al. 2017; an EXor source). Such a difference in the timescales of the rise rates, possibly, implies a different trigger mechanism in Gaia 20eae, resulting in the present luminosity outburst. Once it reached maximum brightness, it slowly started to decay from its maximum brightness with a decay rate of 0.3 mag month^{-1}. The present decay rate is similar to that of the bona fide EXor class of sources, EX Lupi and VY Tau, which returned to its quiescent stages in 1.5–2 years after their maximum brightness state (Herbig 1977). The present decay rate is also similar to that of V899 Mon, which transitioned to a short quiescent state from its 2010 outburst state (Ninan et al. 2015). The decay rate of Gaia 20eae is surprisingly

Table 6
Features of Gaia 20eae Compared to Bona Fide FUors and EXors

Feature	FUor	EXor	Gaia 20eae
Outburst amplitude (mag)	4–6	2–4	4.6
Age	Class I/II	Class II	Class II
Luminosity ($L_{\odot}$)	100–300	0.5–20	5.9
Reflection nebulae	Yes	Sometimes	No
Decay to quiescence	20–100 yr	0.5–2 yr	1.3 yr
Hβ	Absorption	Emission	Absorption
Hα	P Cygni	Emission	P Cygni
CO(2-0) and CO(3-1)	Absorption	Emission	Emission

similar to that of V1118 Ori, being equal to 0.3 mag/month, thus pointing to the fact that a similar relaxing phenomenon is occurring in Gaia 20eae also. During the outburst phase, Gaia 18dvy also shows small-scale fluctuations that have an amplitude of ∼0.2 mag in all of the bands. Such a short scale accretion variability has also been reported by Ninan et al. (2015) for V899 Mon. Similar fluctuations were observed in FU Ori, and may be due to flickering or inhomogeneities in the accretion disk (Kenyon et al. 2000; Siwak et al. 2013; Szegedi-Elek et al. 2020).

A few interesting spectral features of Gaia 20eae are tabulated in Table 6 to classify Gaia 20eae by comparing its property with different classes of the episodic accretion low-mass young stars (Hartmann 1998; Connelley & Reipurth 2018). Most of them match the EXor source, but the Hβ absorption line and P Cygni profile of Hα line hint toward the FUor source classification. The P Cygni profile in Hα originates from the winds generated due to accretion of matter through accretion funnels by the process of magnetospheric accretion. During our spectroscopic monitoring, the P Cygni profile of the Hα line showed substantial variations. We have found that the outflow wind velocity for Gaia 20eae shows a large scatter, which may be due to the intrinsic variation of wind velocity during the outburst phase. As the Hα line originates from the innermost hot zone powered by accretion, the EW of the emission component of the Hα line is an approximate indicator of the accretion rate. Table 5 shows a large variation in the EW values of the Hα line during our monitoring period. Similar to this, the EW of O I λ7773 Å also varied up to ∼75%. This is indicative of the highly turbulent accretion activities going on in Gaia 20eae during its outburst phase. This is also evident from the short scale fluctuations of the photometric magnitudes observed during the same period. These properties of Gaia 20eae are similar to those of the V899 Mon, which also showed heavy outflow activities and an increase in disk turbulence as it transitioned to its quiescent state after its first outburst (Ninan et al. 2015). Therefore, similar to V899 Mon, the present outburst of Gaia 20eae might be triggered by the magnetic instabilities in magnetospheric accretion. Gaia 20eae also clearly shows the decaying phase is less than 15 months, and it also shows the CO bandheads in the emission. These features suggest that Gaia 20eae broadly resembles the EXor family of sources.

Our high-resolution spectrum shows a very strong blue-shifted He λ10830 Å absorption signature, which indicates a very strong outflow activity in Gaia 20eae. We have also detected a redshifted absorption component in all of the Ca II IR triplet lines, which could be due to the hot infalling gas in the magnetospheric accretion funnel. As far as we know, this is the first reported direct detection of an infall signature in Ca II IR triplet lines in the FUors/Exors family of objects. We believe that this is strong evidence for the magnetospheric funnel origin of Ca II IR triplet lines in heavily accreting YSOs. Based on this, we have also constrained the viewing angle such that it is through the accretion funnel to the footprint on the stellar surface.

We thank the anonymous reviewer for valuable comments, which greatly improved the scientific content of the paper. We thank the staff at the 1.3 m DFOT and 3.6 m DOT, Devasthal (ARIES), for their cooperation during observations. It is a pleasure to thank the members of 3.6 m DOT team and IR astronomy group at TIFR for their support during TANSPEC observations. TIFR−ARIES Near Infrared Spectrometer (TANSPEC) was built in collaboration with TIFR, ARIES and MKIR, Hawaii for the DOT. We thank the staff of IAO, Hanle and CREST, Hosakote, that made these observations possible. The facilities at IAO and CREST are operated by the Indian Institute of Astrophysics. This work has made use of data from the European Space Agency (ESA) mission Gaia (https://www.cosmos.esa.int/gaia), processed by the Gaia Data Processing and Analysis Consortium (DPAC, https://www.cosmos.esa.int/web/gaia/dpac/consortium). Funding for the DPAC has been provided by national institutions, in particular the institutions participating in the Gaia Multilateral Agreement. The Center for Exoplanets and Habitable Worlds is supported by the Pennsylvania State University, the Eberly College of Science, and the Pennsylvania Space Grant Consortium. These results are based on observations obtained with the Habitable-zone Planet Finder Spectrograph on the HET. We acknowledge support from NSF grants AST-1006676, AST-1126413, AST-1310885, AST-1310875, ATI 2009889, ATI-2009982, and AST-2108512 in the pursuit of precision radial velocities in the NIR. We acknowledge support from the Heising-Simons Foundation via grant 2017-0494. The Hobby–Eberly Telescope is a joint project of the University of Texas at Austin, the Pennsylvania State University, Ludwig-Maximilians-Universität München, and Georg-August Universität Gottingen. The HET is named in honor of its principal benefactors, William P. Hobby and Robert E. Eberly. The HET collaboration acknowledges the support and resources from the Texas Advanced Computing Center. We thank the Resident astronomers and Telescope Operators at the HET for the skillful execution of our observations with HPF. C.I.C. acknowledges support by NASA Headquarters under the NASA Earth and Space Science Fellowship Program through grant 80NSSC18K1114. S.S., N.P., and R.Y. acknowledge the support of the Department of Science and Technology, Government of India, under project No. DST/INT/Thai/P-15/2019. D.K.O. acknowledges the support of the Department of Atomic Energy, Government of India, under Project Identification No. RTI 4002.

Facilities: HCT (HFOSC), DFOT, DOT (TANSPEC, ADFOSC), ARCSAT, HET (HPF, LRS2).

Software: astropy (Astropy Collaboration et al. 2013), IRAF (Tody 1986, 1993), DAOPHOT-II software (Stetson 1987).

ORCID iDs

Arpan Ghosh https://orcid.org/0000-0001-7650-1870
Saurabh Sharma https://orcid.org/0000-0001-5731-3057
Joe P. Ninan https://orcid.org/0000-0001-8720-5612
Devendra K. Ojha https://orcid.org/0000-0001-9312-3816
Shubham Kanodia https://orcid.org/0000-0001-8401-4300
Suvrath Mahadevan https://orcid.org/0000-0001-9596-7983

Gudmundur Stefansson https://orcid.org/0000-0001-7409-5688
R. K. Yadav https://orcid.org/0000-0002-6740-7425
Tirthendu Sinha https://orcid.org/0000-0001-5508-6575
Neelam Panwar https://orcid.org/0000-0002-0151-2361
John P. Wisniewski https://orcid.org/0000-0001-9209-1808
Caleb I. Cañas https://orcid.org/0000-0003-4835-0619
Andrea S. J. Lin https://orcid.org/0000-0002-9082-6337
Arpita Roy https://orcid.org/0000-0001-8127-5775
Fred Hearty https://orcid.org/0000-0002-1664-3102
Lawrence Ramsey https://orcid.org/0000-0002-4289-7958
Paul Robertson https://orcid.org/0000-0003-0149-9678
Christian Schwab https://orcid.org/0000-0002-0091-7105

References

Aspin, C. 2011, AJ, 141, 196
Astropy Collaboration, Robitaille, T. P., Tollerud, E. J., et al. 2013, A&A, 558, A33
Audard, M., Ábrahám, P., Dunham, M. M., et al. 2014, in Protostars and Planets VI, ed. H. Beuther et al. (Tucson, AZ: Univ. Arizona Press), 387
Bailer-Jones, C. A. L., Rybizki, J., Fouesneau, M., Demleitner, M., & Andrae, R. 2021, AJ, 161, 147
Bellm, E. C., Kulkarni, S. R., Graham, M. J., et al. 2018, PASP, 131, 018002
Cayrel, R. 1988, in IAU Symp. 132, The Impact of Very High S/N Spectroscopy on Stellar Physics, ed. G. Cayrel, G. de Strobel, & M. Spite (Dordrecht: Kluwer), 345
Chambers, K. C., Magnier, E. A., Metcalfe, N., et al. 2016, arXiv:1612.05560
Connelley, M. S., & Reipurth, B. 2018, ApJ, 861, 145
Edwards, S., Fischer, W., Kwan, J., Hillenbrand, L., & Dupree, A. K. 2003, ApJL, 599, L41
Edwards, S., Hartigan, P., Ghandour, L., & Andrulis, C. 1994, AJ, 108, 1056
Faúndez, S., Bronfman, L., Garay, G., et al. 2004, A&A, 426, 97
Gaia Collaboration, Brown, A. G. A., Vallenari, A., et al. 2018, A&A, 616, A1
Gaia Collaboration, Prusti, T., de Bruijne, J. H. J., et al. 2016, A&A, 595, A1
Giannini, T., Antoniucci, S., Lorenzetti, D., et al. 2017, ApJ, 839, 112
Ginsburg, A. 2017, arXiv:1702.06627
Hamann, F., & Persson, S. E. 1992a, ApJS, 82, 247
Hamann, F., & Persson, S. E. 1992b, ApJS, 82, 285
Hankins, M., Hillenbrand, L. A., De, K., et al. 2020, ATel #13902, https://www.astronomerstelegram.org/?read=13902
Hartmann, L. 1998, Accretion Processes in Star Formation (Cambridge: Cambridge Univ. Press)
Hartmann, L., Hewett, R., & Calvet, N. 1994, ApJ, 426, 669
Hartmann, L., & Kenyon, S. J. 1996, ARA&A, 34, 207
Herbig, G. H. 1977, ApJ, 217, 693
Hillenbrand, L. A., Contreras Peña, C., Morrell, S., et al. 2018, ApJ, 869, 146
Hillenbrand, L. A., Reipurth, B., Connelley, M., Cutri, R. M., & Isaacson, H. 2019, AJ, 158, 240
Hodgkin, S. T., Wyrzykowski, L., Blagorodnova, N., & Koposov, S. 2013, RSPTA, 371, 20120239
Kanodia, S., & Wright, J. 2018, RNAAS, 2, 4
Kaplan, K. F., Bender, C. F., Terrien, R., et al. 2019, in ASP Conf. Ser. 523, Astronomical Data Analysis Software and Systems XXVIII, ed. P. J. Teuben et al. (San Francisco, CA: ASP), 567
Kenyon, S. J., Kolotilov, E. A., Ibragimov, M. A., & Mattei, J. A. 2000, ApJ, 531, 1028
Lomb, N. R. 1976, Ap&SS, 39, 447
Mahadevan, S., Ramsey, L., Bender, C., et al. 2012, Proc. SPIE, 8446, 84461S
Mahadevan, S., Ramsey, L. W., Terrien, R., et al. 2014, Proc. SPIE, 9147, 91471G
McGehee, P. M., Smith, J. A., Henden, A. A., et al. 2004, ApJ, 616, 1058
Metcalf, A. J., Fredrick, C. D., Terrien, R. C., Papp, S. B., & Diddams, S. A. 2019, OptL, 44, 2673
Muzerolle, J., Hartmann, L., & Calvet, N. 1998, AJ, 116, 455
Ninan, J. P., Bender, C. F., Mahadevan, S., et al. 2018, Proc. SPIE, 10709, 107092U
Ninan, J. P., Ojha, D. K., Baug, T., et al. 2015, ApJ, 815, 4
Ninan, J. P., Ojha, D. K., Bhatt, B. C., et al. 2013, ApJ, 778, 116
Ojha, D., Ghosh, S. K., Sharma, S., et al. 2018, BSRSL, 87, 58
Peeters, E., Spoon, H. W. W., & Tielens, A. G. G. M. 2004, ApJ, 613, 986
Ramsey, L. W., Adams, M. T., Barnes, T. G., et al. 1998, Proc. SPIE, 3352, 34
Retes-Romero, R., Mayya, Y. D., Luna, A., & Carrasco, L. 2017, ApJ, 839, 113
Robitaille, T. P., Meade, M. R., Babler, B. L., et al. 2008, AJ, 136, 2413
Safron, E. J., Fischer, W. J., Megeath, S. T., et al. 2015, ApJL, 800, L5
Scargle, J. D. 1982, ApJ, 263, 835
Scholz, A., Froebrich, D., & Wood, K. 2013, MNRAS, 430, 2910
Sharma, S., Ghosh, A., Ojha, D. K., et al. 2020, MNRAS, 498, 2309
Shetrone, M., Cornell, M. E., Fowler, J. R., et al. 2007, PASP, 119, 556
Sinha, T., Sharma, S., Pandey, A. K., et al. 2020, MNRAS, 493, 267
Siwak, M., Rucinski, S. M., Matthews, J. M., et al. 2013, MNRAS, 432, 194
Stefansson, G., Cañas, C., Wisniewski, J., et al. 2020, AJ, 159, 100
Stetson, P. B. 1987, PASP, 99, 191
Szegedi-Elek, E., Ábrahám, P., Wyrzykowski, Ł., et al. 2020, ApJ, 899, 130
Tody, D. 1986, Proc. SPIE, 627, 733
Tody, D. 1993, in ASP Conf. Ser., 52, IRAF in the Nineties, ed. R. J. Hanisch, R. J. V. Brissenden, & J. Barnes (San Francisco, CA: ASP), 173
Tonry, J. L., Stubbs, C. W., Lykke, K. R., et al. 2012, ApJ, 750, 99
Vorobyov, E. I., & Basu, S. 2006, ApJ, 650, 956
Wyrzykowski, Ł., Hodgkin, S., Blogorodnova, N., Koposov, S., & Burgon, R. 2012, in Proc. 2nd Gaia Follow-up Network for Solar System Objects, ed. W. Thuillot et al. (Paris: IMCCE), 21